Molecular Therapy
Advances
Original Article

Spatial mapping of barcoded, brain-tropic AAVs using multiplexed RNA *in situ* hybridization

Youssef Fouani,[1] Martin Oti,[2] Sebastian Jarosch,[3] Dragica Blazevic,[1] Matthias Johannes Duechs,[1] Stephanie Ketterer,[1] Robert Becker,[1] Sarah Abele,[3] Benjamin Strobel,[3] Tanja Schoenberger,[3] Gregorio Alanis-Lobato,[2] Werner Rust,[3] Christian Schoen,[1] Matthias Klugmann,[1] Udo Maier,[1] Jonas Doerr,[3] and Stefan Michelfelder[1]

[1]Eye Health & Research Beyond Borders, Boehringer Ingelheim Pharma GmbH & Co. KG, 88397 Biberach an der Riss, Germany; [2]Computational Innovation, Boehringer Ingelheim Pharma GmbH & Co. KG, 88397 Biberach, Germany; [3]Drug Discovery Sciences, Boehringer Ingelheim Pharma GmbH & Co. KG, 88397 Biberach an der Riss, Germany

Gene therapy cargo delivery to specific cell types in the central nervous system (CNS) remains a major challenge for the development of adeno-associated virus (AAV) vectors as a therapeutic modality. Here, we leverage high-plex *in situ* transcriptomics (10× Genomics Xenium) to spatially map barcoded AAV payloads at subcellular resolution in the intact mouse brain while preserving anatomical context. Tropism profiling of 22 barcoded AAV variants including novel AAV9 derivatives and CNS-targeted capsids revealed that established vectors, AAV9-PHP.eB and AAV9-CAP-B10, demonstrated distinct neuronal and non-neuronal subtype preferences, recapitulating previous findings. Several novel AAV variants candidates predominantly transduced endothelial and vascular cells, suggesting limited blood-brain barrier (BBB) penetration. Notably, three novel variants (AAV9-BTX166, -BTX168, and -BTX175) exhibited enhanced endothelial and mural cell tropism, despite robust CNS activity in bulk assays. Intriguingly, the novel variants AAV9-BTX149 and -BTX001 displayed selective targeting of specific inhibitory neuron subtypes, with a single Trp503Arg substitution in the capsid being sufficient to redirect tropism. Our results establish *in situ* spatial transcriptomics as a powerful tool for resolving AAV biodistribution and BBB traversal capacities at high resolution, providing a blueprint for capsid engineering to achieve precise cell subtype targeting in the CNS.

INTRODUCTION

The human blood-brain barrier (BBB) is a highly selective and tightly regulated biological interface that protects the central nervous system (CNS) from potential pathogens and toxins in the blood. However, this protective barrier presents a significant challenge for the non-invasive delivery of gene therapy, particularly using adeno-associated virus (AAV) vectors, which have become central to the development of gene therapies for neurological diseases. Therefore, the restrictive nature of the BBB necessitates the administration of high doses of vectors to achieve effective CNS transduction and therapeutic outcomes. This, in turn, increases the risk of systemic toxicity and off-target effects.[1–5]

To circumvent this challenge, strategies have been devised to enhance both the efficiency and specificity of AAV-mediated gene delivery to the CNS.[6–10] One major focus has been engineering AAV capsids to improve their tropism for CNS tissues and facilitate more efficient BBB crossing to precisely target neural and non-neuronal cell populations.[11–15] Over the past two decades, high-throughput AAV engineering platforms have accelerated the discovery of novel capsids in various species,[16,17] such as rodents and non-human primates (NHPs).[13,18] In this context, innovative high-throughput screening strategies, such as CREATE[11] and M-CREATE,[12] have utilize randomized peptide-display library technology and Cre-recombinase-dependent selection strategies to generate AAV variants with improved CNS targeting and refined cell-type specificity.[16,17,19–21] Notable examples emerging from both platforms include AAV9-PHP.B[11] and AAV9-PHP.eB,[12] which have repeatedly demonstrated remarkable CNS tropism in preclinical models. More recently, a new generation of high-throughput screening platforms has emerged. Technologies such as TRACER,[13] iTransduce,[14] BRAVE,[15] and DELIVER,[22] employ strategies that incorporate cell type-specific regulatory elements, enabling the identification and selection of AAV variants with cell type-specific functional applications in complex tissues. Ultimately, these efforts have led to the development of AAV variants with tailored tropism, capable of selectively targeting not only the CNS but also the peripheral nervous system and specific neuronal or glial subpopulations.[11,12,14,23–25]

Received 26 September 2025; accepted 9 February 2026;
https://doi.org/10.1016/j.omta.2026.201693.

Correspondence: Dr. Stefan Michelfelder, Eye Health & Research Beyond Borders, Boehringer Ingelheim Pharma GmbH & Co. KG, Biberach an der Riss 88397, Germany..
E-mail: stefan.michelfelder@boehringer-ingelheim.com

Despite these technological advances, the comprehensive characterization of AAV tropism remains a significant bottleneck in the field. It has become increasingly evident that AAV tropism observed in one species does not always translate to others, underscoring the critical need for robust and predictive evaluation methods that can bridge the gap between animal models and human biology.[26,27] Moreover, traditional approaches, including bulk tissue analytics lack the resolution required to dissect cell type-specific AAV transduction and expression profiles.[28,29] Histological analytics, while offering spatial resolution, are inherently low-throughput and lack the multiplexing capacity to compare, at scale, the cellular and subcellular profiles of multiple AAV variants. Advanced single-cell RNA sequencing (scRNA-seq) has improved our ability to profile AAV expression at high resolution;[30,31] nevertheless, it comes at the cost of losing spatial information, which is crucial for understanding the distribution and behavior of viral vectors within the complex architecture of the brain.

Spatial transcriptomics enables the simultaneous acquisition of high-resolution expression profiles in a spatial context within intact tissues,[32–34] allowing the detailed mapping of AAV variant performance to the subcellular level and providing insights into their tropism and expression efficacy.[35] Recent adaptations of spatial transcriptomics have expanded its utility, allowing the *in situ* evaluation of complex barcoded AAV libraries within intact tissue.[35,36]

In the present study, we leveraged the capabilities of the 10× Genomics Xenium *in situ* platform to investigate the spatial distribution and cellular tropism of a barcoded pool of 22 distinct AAV variants. Our pool included both recombinant and natural AAVs, with each variant characterized by unique tropism, expression efficiency, and specificity to mouse brain tissue. Along with AAV2, AAV9, and AAV9 Trp503Arg (AAV9W503R), we analyzed the well-established CNS-tropic benchmarks; AAV9-PHP.eB,[12] its derivatives AAV9-CAP-B10 and AAV9-GNSSKQF,[18] AAV9P31,[13] and AAV-F.[14] Furthermore, the barcoded AAV library also included 14 novel AAV9 variants, each engineered to display peptides inserted at the AA588 loop of either the AAV9 or AAV9W503R backbone.[37] These novel variants were isolated through iterative screening of 7-mer and 12-mer display libraries in C57Bl/6NCrl mice to identify candidates exhibiting enhanced CNS tropism.

Utilizing single-oligonucleotide probes targeting the unique AAV barcodes, along with a pre-designed 248-gene mouse brain gene expression panel, the 10× Genomics Xenium platform enabled high-resolution profiling of AAV variant transduction across both neuronal and non-neuronal brain cell populations.

Overall, our study highlights the transformative potential of the 10× Genomics Xenium *in situ* transcriptomics platform for the functional analysis and characterization of AAV variants. By enabling comprehensive cell subtype profiling within the spatial context of intact brain tissue, this approach paves the way for the selection and profiling of next-generation AAV vectors with optimized cell type-specific targeting properties for CNS gene therapy.

RESULTS

Novel AAV9 variants demonstrate enhanced brain tropism in mice

In this study, we identified a panel of novel AAV9 variants—referred to as AAV9-BTX, a brain-targeted gene therapy vector—through *in vivo* screening of AAV9 peptide display libraries. These variants demonstrated enhanced enrichment in the mouse CNS. To identify them, we constructed two randomized AAV9 peptide display libraries and screened for brain-tropic variants. The first library displayed 7-mer peptides (theoretical diversity: 1.28E+09) inserted into loop VIII of Cap AAV9-W503R using the SfiI restriction site at ($Q_{588}A_{589}G_{590}(NNK)_7A_{591}Q_{592}A_{593}$). AAV9-W503R has previously been shown to reduce liver tropism (Figure 1A).[37] The second library displayed 12-mer peptides (theoretical diversity: 4.10E+15), inserted at the same position ($Q_{588}A_{589}G_{590}(NNK)_{12}A_{591}Q_{592}A_{593}$) into loop VIII of AAV9. Next-generation sequencing (NGS) confirmed the diversity of both plasmid (P0) and viral (V0) input libraries (Figures 1A, S1A, and S1B).

NGS-guided *in vivo* screenings were performed by intravenous administration via the tail vein of each library into female C57BL/6NCrl mice at a dose of 5E+13 vg/kg. Across iterative rounds of selection, we observed progressive enrichment of AAV9 variant genomes in the brain. For the AAV9-W503R 7-mer library, sequences recovered from brain tissue after round 3 strongly filtered toward a limited set of variants (Figures 1B and S1A). Top candidates included NRRPDDM (AAV9-BTX001), NMIRQQE (AAV9-BTX003), NITKYQE (AAV9-BTX005), NYTKSQP (AAV9-BTX007), and NTSKNLA (AAV9-BTX009), each showing substantial fold enrichment compared to their initial abundance in the viral pool (R0), (Figures 1B and 1D, S1A, and Table S1). Similarly, the AAV9-WT 12-mer library yielded distinct variants, with leading candidates such as HWNGSQLKYKDQ (AAV9-BTX166), LYDNKARKWPED (AAV9-BTX167), HYTIQAGYRGDA (AAV9-BTX168), and VYDEANYKYNHP (AAV9-BTX169) dominating the pool of CNS-tropic AAV9 variants recovered from the brain after three rounds (Figures 1C and 1E, S1B, and Table S2).

Among the heptamer variants, HPHIDKA (AAV9-BTX033), NSTKYQE (AAV9-BTX027), YLHYTEP (AAV9-BTX002), and TKWTAYN (AAV9-BTX024) displayed strong bias toward the brain relative to other organs (Figure 1F). The most abundant variant, NRRPDDM (AAV9-BTX001), showed additional tropism for the heart and lung while detargeting the liver (Figure 1F). In contrast, the top 12-mer variants—HWNGSQLKYKDQ (AAV9-BTX166), LYDNKARKWPED (AAV9-BTX167), and HYTIQAGYRGDA (AAV9-BTX168)—exhibited a stronger bias profile compared to their top AAV9-heptamer counterparts, with pronounced brain targeting and minimal off-target distribution in the liver, heart, lung, muscle, kidney, and spleen (Figure 1G).

Selected AAV9 candidates were vectorized as recombinant AAVs carrying an enhanced green fluorescent protein (eGFP) reporter driven by the ubiquitous a cytomegalovirus (CMV) promoter to enable individual *in vivo* validation. These included three 7-mer

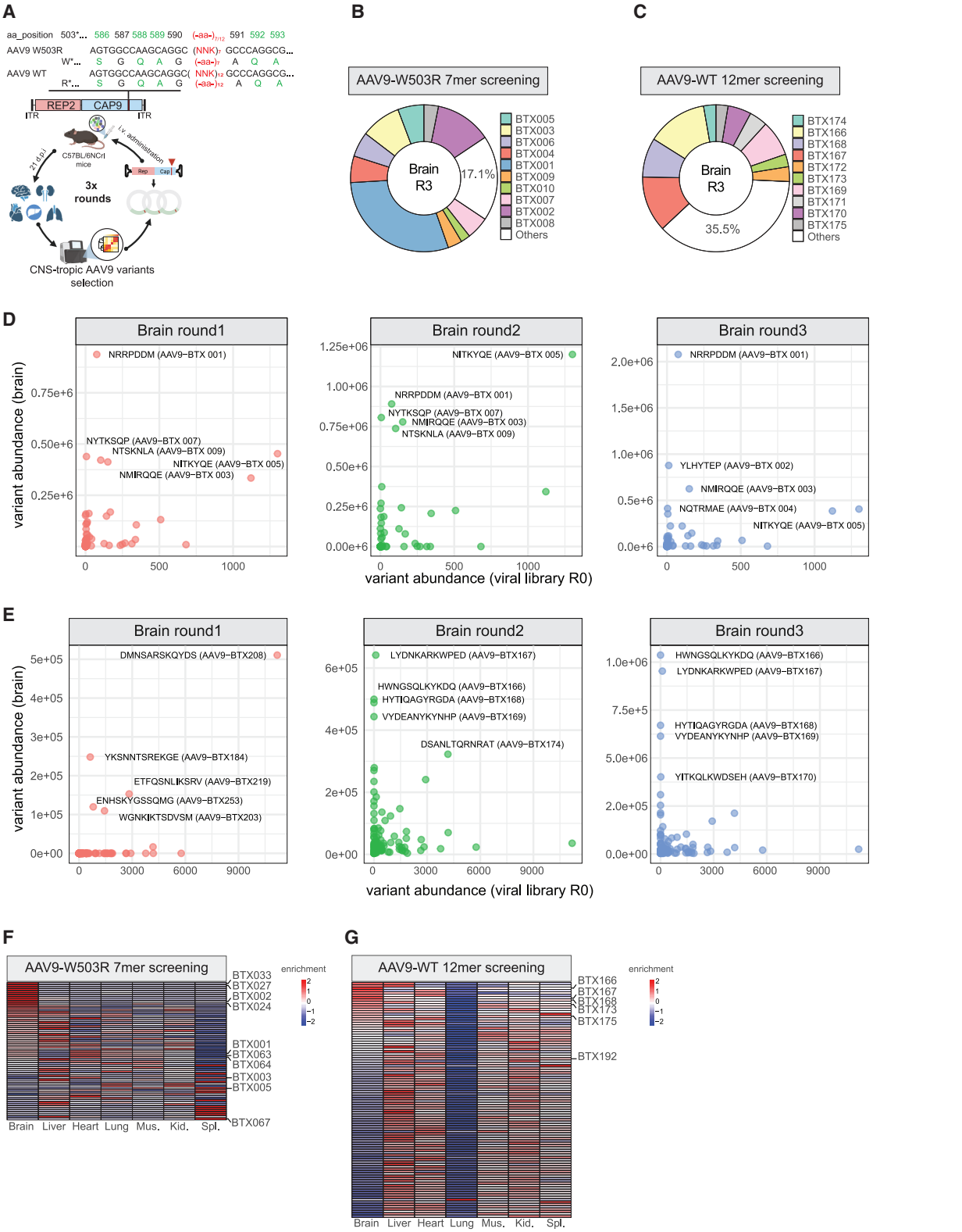

(legend on next page)

insertion variants—AAV9-BTX001, BTX002, and BTX024—along with AAV9-BTX149, and five 12-mer insertion variants—BTX166, -BTX168, -BTX173, -BTX175, and -BTX192. Individual vectors were systemically administered into female C57BL/6NCrl mice (n = 3) at a total dose of 1E+11 viral genomes (vg) per mouse, and three weeks post-injection, we assessed the transduction capacity and bioactivity of each vector in the brain and liver relative to benchmark vectors AAV9 and AAV9-PHP.eB. All novel variants, except AAV9-BTX001, exhibited higher brain transduction efficiency than AAV9, whereas all variants, including AAV9-BTX001, outperformed AAV9 in driving eGFP expression in the brain (Figure S2A). In this context, the 12-mer variants AAV9-BTX166, -BTX168, and -BTX173 achieved the most robust expression among all novel variants, showing an ∼11- to 13-fold increase over AAV9 (Figure S2A). Among the 7-mer variants, AAV9-BTX002 and -BTX024 drove the strongest expression, achieving ∼7.8 -fold and ∼4.5-fold increases in eGFP expression compared to AAV9. In the liver, AAV9-PHP.eB, -BTX149, and -BTX175 exhibited higher transduction than other novel variants; however, all novel AAVs and PHP.eB showed reduced eGFP expression compared to AAV9 (Figure S2B).

Subsequently, we expanded the set of tested variants to include additional candidates exhibiting enhanced brain tropism. Accordingly, 14 novel AAV9 variants were vectorized (Figure 2A), alongside reference vectors AAV2, AAV9, and AAV9-W503R.[37] Of these, six variants—AAV9-BTX166, -BTX167, -BTX168, -BTX173, -BTX175, and -BTX192—were derived from the AAV9-12-mer library screening. The remaining eight were AAV9-7mer variants, including AAV9-BTX001, -BTX002, -BTX003, -BTX011, -BTX013, -BTX024, and -BTX063, all engineered on the AAV9-W503R backbone. To further assess the impact of peptide context, we also implemented the most abundant heptamer variant, AAV9-BTX001 (NRRPDDM), onto a wild-type AAV9 backbone, generating AAV9-BTX149 (Table S3). In addition, we included 5 previously reported and well-established CNS-tropic AAV9 variants: AAV-PHP.eB,[12] CAP-B10, GNSSKQF;[18] AAV-F;[14] and AAV9P31.[13]

Each AAV variant was vectorized to encapsulate an eGFP reporter cargo, barcoded with a 15-nucleotide sequence (Figure 2A).[28] The 22 barcoded AAVs were produced individually and then mixed to achieve an equimolar ratio (Figure 2B). This pooled library was administered intravenously into female C57BL/6NCrl mice (n = 3) at a total dose of 1E+12 vg/mouse. Three weeks post-injection, DNA and RNA were isolated from the brain and liver, followed by NGS to assess viral genome abundance and transcriptional activity (Figure 2A). Additionally, we quantified the viral genome abundance of individual variants in the input library, which revealed deviations from the intended equimolar composition (Figure 2B). To account for this, viral genome abundance and cargo expression levels in target tissues were normalized to the relative representation of each variant within the input pool.

Of the evaluated AAV variants, 13 exhibited enhanced brain transduction compared to AAV9 and AAV9W503R (Figure S2C). Notably, AAV9P31 and the novel variant AAV9-BTX166 achieved an approximately 40-fold increase in barcoded cargo delivery relative to AAV9. All 12-mer AAV9 variants, with the exception of AAV9-BTX167, demonstrated reduced liver tropism, with AAV9-BTX175 and AAV9-BTX173 showing the strongest liver detargeting among the engineered AAV9-BTX variants (Figure S2D). Among the 7-mer variants, only AAV9-BTX001, AAV9-BTX002, and AAV9-BTX024 exhibited lower liver targeting than AAV9.

Transcriptionally, AAV9P31 exhibited the highest brain barcode expression, exceeding parental AAV9 by 25-fold (Figure 2C). AAV-PHP.eB and its derivatives, CAP-B10 and GNSSKQF,[18] achieved an 8- to 15-fold increase in brain expression relative to AAV9. In total, 9 variants demonstrated at least a 2-fold increase in specific brain expression compared to AAV9, with CAP-B10 achieving a strong brain-to-liver expression ratios, followed by PHP.eB, AAV9-BTX166, -BTX173, and AAV9P31(Figures 2C, 2D, and S2E). Among the novel candidates, only five—AAV9-BTX166, -BTX173, -BTX168, -BTX175, and -BTX002—outperformed AAV9 in brain transcriptional activity (Figure 2C). In contrast, AAV9-BTX013, -BTX003, -BTX063, and -BTX001 showed the lowest brain transcriptional activity, reaching only about 10% of the levels observed with AAV9 (Figure 2C). Most of the tested variants demonstrated at least a 10% reduction in liver transcriptional activity compared to AAV9. Moreover, 9 variants exhibited reduced cargo expression relative to AAV9W503R; these include the novel variants AAV9-BTX175, -BTX173, and -BTX166, with CAP-B10 displaying the lowest liver expression (Figure 2D).

Collectively, these results demonstrate the successful identification of multiple novel AAV9-derived capsids with substantially enhanced brain specificity and reduced liver expression compared to parental AAV9, thereby expanding the toolkit for efficient and targeted CNS gene delivery in mice.

Novel AAV9-BTX002, -BTX168, and -BTX173 variants exhibit cross-strain brain tropism

AAV-PHP.B and PHP.eB capsids efficiently transduce the CNS in C57BL/6NCrl mice, primarily by relying on the Ly6A receptor, whose expression varies among mouse strains—being highly expressed in C57BL/6NCrl mice and low in BALB/c mice. This receptor expression dependency results in markedly reduced gene delivery in BALB/c mice.[38–40]

Figure 1. Identification of novel brain-targeted AAV9 variants through *in vivo* peptide library screening

(A) Schematic overview of *in vivo* selection and library design, showing insertion of randomized 7-mer or 12-mer peptides into loop VIII of the AAV9 capsid. The 7-mer library was built on an AAV9-W503R backbone, while the 12-mer library used wild-type AAV9. Relative abundance of top-10 enriched AAV9 variants in round 3 of screening of (B) AAV9-W503R 7-mer and (C) AAV9-WT 12-mer libraries. Progressive enrichment of (D) AAV9-W503R 7-mer and (E) AAV9-WT 12-mer variants in the brain over 3 rounds of *in vivo* screening. Biodistribution analysis of the leading (F) 7-mer and (G) 12-mer variants in the brain compared to peripheral organs.

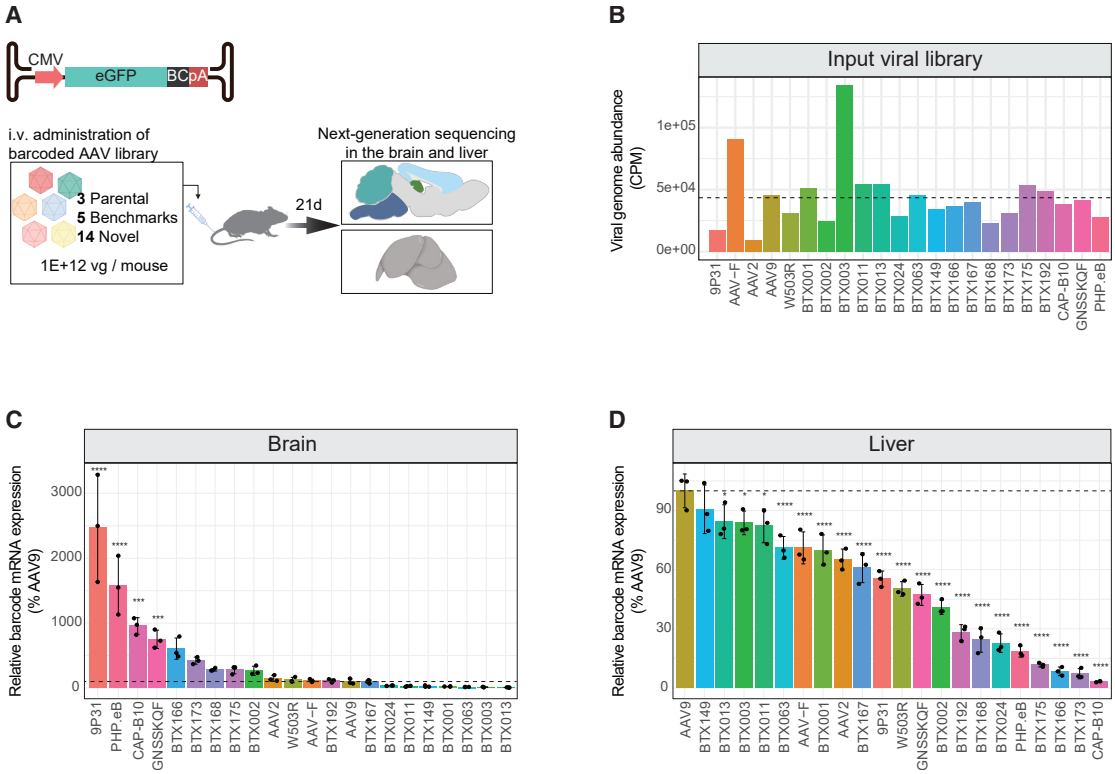

Figure 2. Assessment of barcoded AAV capsid variants for efficiency and specificity of gene expression in C57BL/6NCrl mouse brain

(A–G) Overview of the workflow for barcoded AAV-library testing *in vivo*. Each of the 22 AAV variants encapsulated a single barcoded eGFP reporter gene driven by a CMV promoter. The barcoded AAV library was administered intravenously via the tail vain at a dose of 1E+12 vg/mouse. Three weeks post-injection, animals were euthanized, and the brain and liver tissues were quantified for barcoded DNA and mRNA enrichment using NGS.

(B) Individual barcoded AAV abundance in the input viral library. The dashed line indicates the expected equimolar level of all variants within the library. NGS-based comparison of barcoded cargo mRNA expression levels relative to the parental AAV9 variant in the mouse (C) brain and (D) liver. Variants are ranked in descending order based on relative expression. $n = 3$ independent biological replicates. Data are represented as mean ± SEM. Hereafter, W503R = AAV9W503R, PHP.eB = AAV9-PHP.eB, CAP-B10 = AAV9-CAP-B10, GNSSKQF = AAV9-GNSSKQF. Statistical significance compared to AAV9 was determined using one-way ANOVA with Dunnett's test for multiple comparisons. $^{*}p < 0.05$, $^{***}p < 0.0005$, $^{****}p < 0.0001$.

CPM, count per million

To assess whether our novel variants could overcome strain-specific restrictions, we assembled a barcoded AAV library consisting of 12 variants. This library included four novel AAV9 capsids (AAV9-BTX002, -BTX024, -BTX168, and -BTX173), representing the top two performing 7-mer and 12-mer variants in the brain based on their transcriptional performance both individually (Figure S2A) and in the barcoded library screen (Figure 2C); the three parental vectors (AAV9, AAV9W503R, and AAV2); and the five benchmark vectors used in the previous screening. This library was administered intravenously into female C57BL/6NCrl and BALB/c mice ($n = 3$) at a total dose of 1E+12 vg/mouse. Three weeks post-injection, brain and liver tissues were harvested for barcoded DNA and mRNA quantification via NGS (Figure S2F).

In C57BL/6NCrl mice, AAV9-BTX002, -BTX168, and -BTX173 demonstrated enhanced CNS tropism and cargo expression, with a 2- to 5-fold increase in brain eGFP expression compared to AAV9 (Figure S2G, C57BL/6), along with effective liver detargeting (Figure S2H, C57BL/6). IN contrast, AAV9-BTX024 showed lower cargo expression in the brain compared to any parental AAV. Benchmark vectors AAV9P31, PHP.eB, and CAP-B10 delivered the highest increases in brain eGFP mRNA expression (Figure S2G, C57BL/6)—50-, 33-, and 16-fold, respectively, over AAV9—while also reducing liver expression (Figure S2H, C57BL/6).

In BALB/c mice, the novel variants AAV9-BTX002, -BTX168, and -BTX173 achieved 2- to 5-fold higher brain eGFP expression relative to AAV9 (Figure S2G, BALB/c). In the liver, AAV9-BTX002, -BTX024, and -BTX173 demonstrated the lowest expression (Figure S2H, BALB/c). Among benchmark vectors, AAV9P31 consistently drove efficient barcoded cargo delivery and expression in the brain compared to AAV9. In contrast, PHP.eB and its derivatives CAP-B10 and GNSSKQF failed to drive eGFP expression in the BALB/c brain (Figure S2G, BALB/c).

These findings suggest that the brain-targeting properties of AAV9-BTX002, -BTX168, -BTX173, and AAV9P31 are potentially mediated by mechanisms distinct from those used by PHP.eB and CAP-B10 in C57BL/6 mice.[38–40] Therefore, dedicated mechanistic studies will be necessary to define the receptor(s) and pathways engaged by these novel variants in both C57BL/6 and BALB/c mice.

Barcoded transcripts are readily detected in AAV-transduced cells *in vitro*

Next, we assessed the 10× Genomics Xenium *in situ* transcriptomics workflow for its ability to specifically and efficiently detect barcoded cargo transcripts in AAV-transduced AC16 cells *in vitro*. To this end, cells were transduced with individual AAV variants (AAV9W503R, AAV2, AAV9, AAV9-BTX002, -BTX024, -BTX168, -BTX173, CAP-B10, GNSSKQF, AAV9P31, and AAV-F), as well as with a pooled viral library (AAV9-BTX168, -BTX173, CAP-B10, GNSSKQF, AAV9P31, and AAV-F) at multiplicity of infection (MOI) of 2E+5. To enable AAV multiplexing, we designed unique padlock probes for each barcode to ensure specific detection. In addition, we included three probes targeting eGFP, seven targeting the CMV promoter, and one targeting the invert terminal repeat (ITR) (Figure 3A), all serving as transduction controls. Forty-eight hours post-transduction, individual padlock probes successfully detected each barcode, enabling multiplexed analysis of the transduced AAV variants.

All AAV variants efficiently transduced cells, with ≥80% of cells positive for eGFP or CMV (Figures 3B and 3C). AAV2 yielded the highest proportions of eGFP- and CMV-positive cells (Figures 3B and 3C). CMV and GFP signals colocalized in >90% of cells (Figures 3D, 3E, and S3A). eGFP-positive cells also co-expressed COL1A1, PRPH, NR2F2, and FN1 (Figure S3A). Detection of viral DNA via the ITR probe was less efficient than with CMV: ∼20% of AAV9W503R-BC01 cells and 80% of AAV2-BC02 cells were ITR-positive (Figure S3B).

Except for AAV9-BXT173, all single barcode-targeting probes efficiently detected their respective targets in ≥80% of on-target cells, with limited signal in off-target cells (Figures 3F and 3G). Moreover, all barcode-targeting probes, except BC15 (Figure S3C), displayed a high degree of specificity, as evidenced by their relatively low cross-reactivity with off-target barcodes (0.55%–3.62%; Figure 3F, multi). As mentioned earlier, all barcodes except BC30 (AAV9-BTX173) were detected in ≥80% of their respective transduced cells (Figures 3F and 3G). The BC30-targeting probe detected only ∼56% of AAV9-BTX173-BC30 cells (Figure 3F), despite >85% being eGFP- and CMV-positive (Figures 3B and 3C).

In pooled library-transduced cells, BC29, BC30, BC33, BC34, BC35, and BC36 were efficiently and specifically detected. Among barcode-positive cells, 46.3% expressed multiple barcodes (Figure 3F). AAV9-BTX173-BC30 and AAV9P31-BC35 accounted for the smallest fractions (∼10% and ∼14.7%, respectively), while other barcodes represented ≥20% of barcode-positive cells.

In summary, single barcode-targeting probes within the Xenium platform enabled specific and efficient detection of barcoded cargos in AAV-transduced cells *in vitro*, with minimal nonspecific cross-reactivity.

Spatial profiling of barcoded AAV library in mouse brain

To demonstrate the high-resolution multiplexed profiling capabilities of the Xenium *in situ* platform, we analyzed cell-type tropism of 22 AAV variants in the left hemisphere of three mice injected systemically with a barcoded AAV panel (Figures 2A and 4A). In total, we profiled approximately 510,000 cells (about 169,000 cells per section) *in situ*, quantifying the spatial expression of individual barcodes across both neuronal and non-neuronal cell populations.

Using the 248-gene Xenium mouse brain gene expression panel (Figure 4B, Table S4), cells were classified into 39 distinct clusters (Figures 4C and 4D). Cluster and cell-type assignments in the spatial data were based on scRNA-seq reference clusters,[41,42] and the Allen Brain Atlas (Figure S4A).[43]

The resulting classification included 10 inhibitory neuron types, 13 excitatory neuron types, 9 hippocampal neuron types, and 7 non-neuronal cell types. Excitatory neuronal subtypes were annotated as cortical layer neurons according to the cortex and hippocampus scRNA-seq reference data, which led to excitatory neurons in non-cortical regions also receiving cortical annotations due to reference limitations. Non-neuronal clusters comprised oligodendrocytes, astrocytes, endothelial cells, smooth muscle cells and pericytes (SMC/pericytes), vascular leptomeningeal cells (VLMCs), and microglia (Figures 4C, 4D, and S4A). Due to constraints in the reference dataset, cerebellar neurons were annotated as Cajal-Retzius (CR) cells (Figures 4C and 4D).

Among non-neuronal cells, astrocytes (∼35,000), oligodendrocytes (∼20,000), and endothelial cells (∼12,500) were the most abundant (Figure S4B). The dominant inhibitory neuron subtypes were myeloid ecotropic viral integration site 1 homolog 2 (Meis2+), parvalbumin (Pvalb+), and somatostatin (Sst+) (∼500 cells each), while the most common excitatory neurons were L2.3.IT (Slc17a7+/Cpne6+) and L2.IT (Slc17a7+/Pkib+), each with ∼10,000 cells (Figure S4B). Hippocampal neurons were the least abundant, with vasoactive intestinal peptide (Vip+) and CA2 subtypes at ∼100 cells each (Figure S4B). Although previous large-scale single-cell and spatial transcriptomics studies have characterized the diversity of hippocampal neurons,[42,44] quantitative cell-type abundance varies across platforms and experimental designs, limiting direct comparisons.

After clustering based on endogenous gene expression, we quantified AAV transduction across cell types. eGFP mRNA was detected in ∼12,700 cells, the CMV promoter in ∼7,700 cells, and barcodes in ∼7,000 cells (Figures 5A, 5B, S5A, and S5C). Viral ITRs were detected less frequently, in ∼700 cells, consistent with our *in vitro* findings (Figures 5A and S6A). eGFP was detected more frequently than

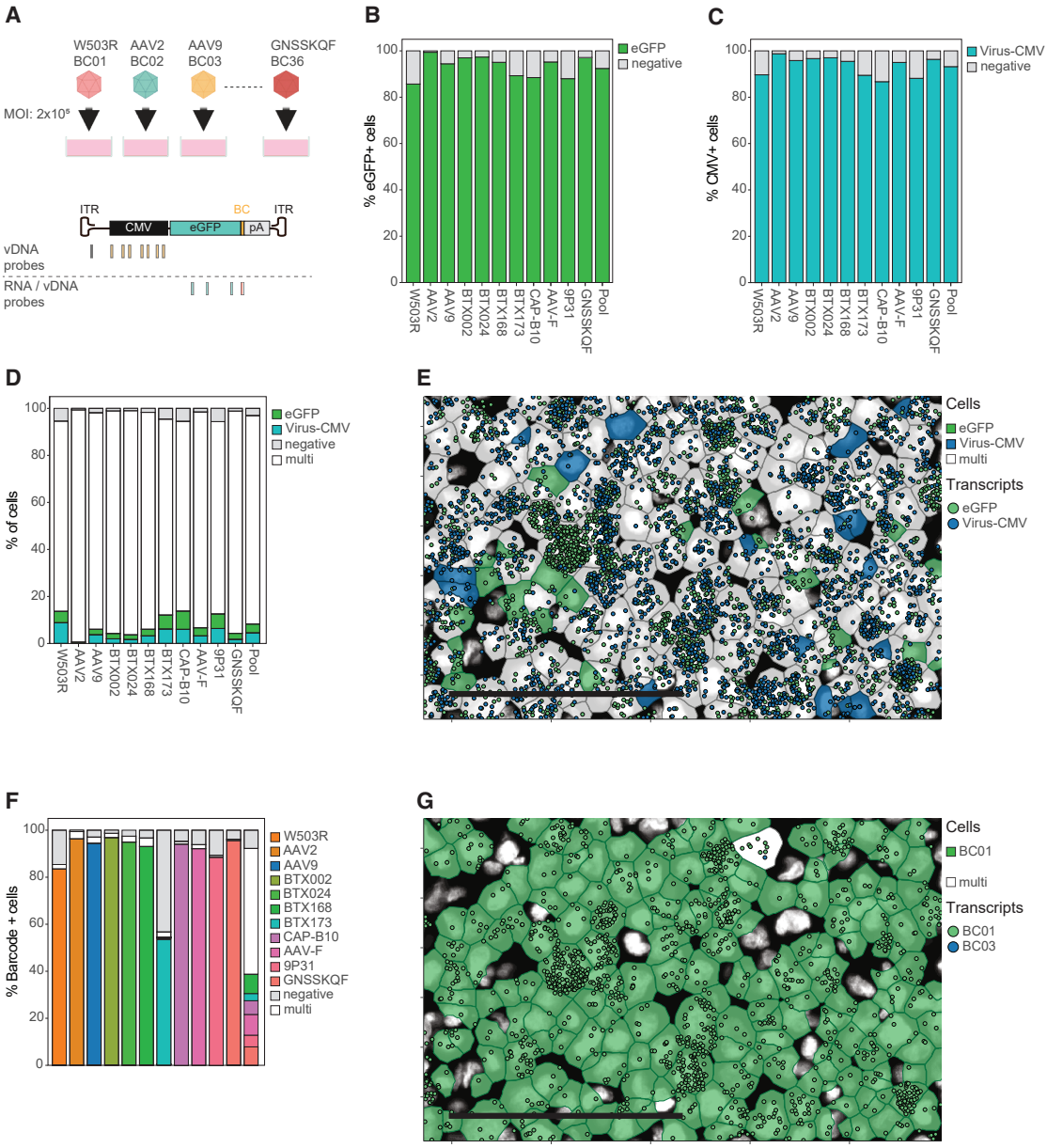

Figure 3. *In vitro* evaluation of padlock probe-based detection of AAV variants

(A–D) Overview of the workflow for *in vitro* padlock probe-based detection of AAV variants. Cells were transduced with AAVs either individually or as panels at an MOI of 2E+5. Forty-eight hours post-transduction, individual AAV variants were detected using single barcoded-targeting probes. Additionally, the CMV promoter, eGFP gene, and ITRs were targeted using 7, 3, and 1 probe(s), respectively. Percentages of (B) eGFP-positive cells, (C) CMV-positive cells, and (D) cells showing colocalization of eGFP and CMV signals are shown.

(E) Detection of eGFP gene (green) and CMV promoter (blue) *in vitro*. eGFP and CMV double-positive cells are indicated in white. Nuclei were stained with DAPI (gray). ∼250 cells are depicted.

(F) Detection of AAV barcoded transcripts *in vitro* using one probe per barcode. All barcodes, except BXT173-BC30, were detected in ≥80% of transduced cells with minor cross-reactivity (white). In pool transduced cells, ≥90% of cells were transduced, with ∼50% of cells transduced with more than one barcoded AAV (pool; white).

(G) Detection of cross-reactivity of BC03 (blue) with BC01 (green) in AAV9W503R-BC1 transduced cells *in vitro*. BC01-positive cells are indicated in green, and BC01 and BC03 double-positive cells are indicated in white. Nuclei were stained by DAPI (gray). $n = 1$. ∼250 cells are depicted. Scale bars, 100 μm.

vDNA, viral DNA

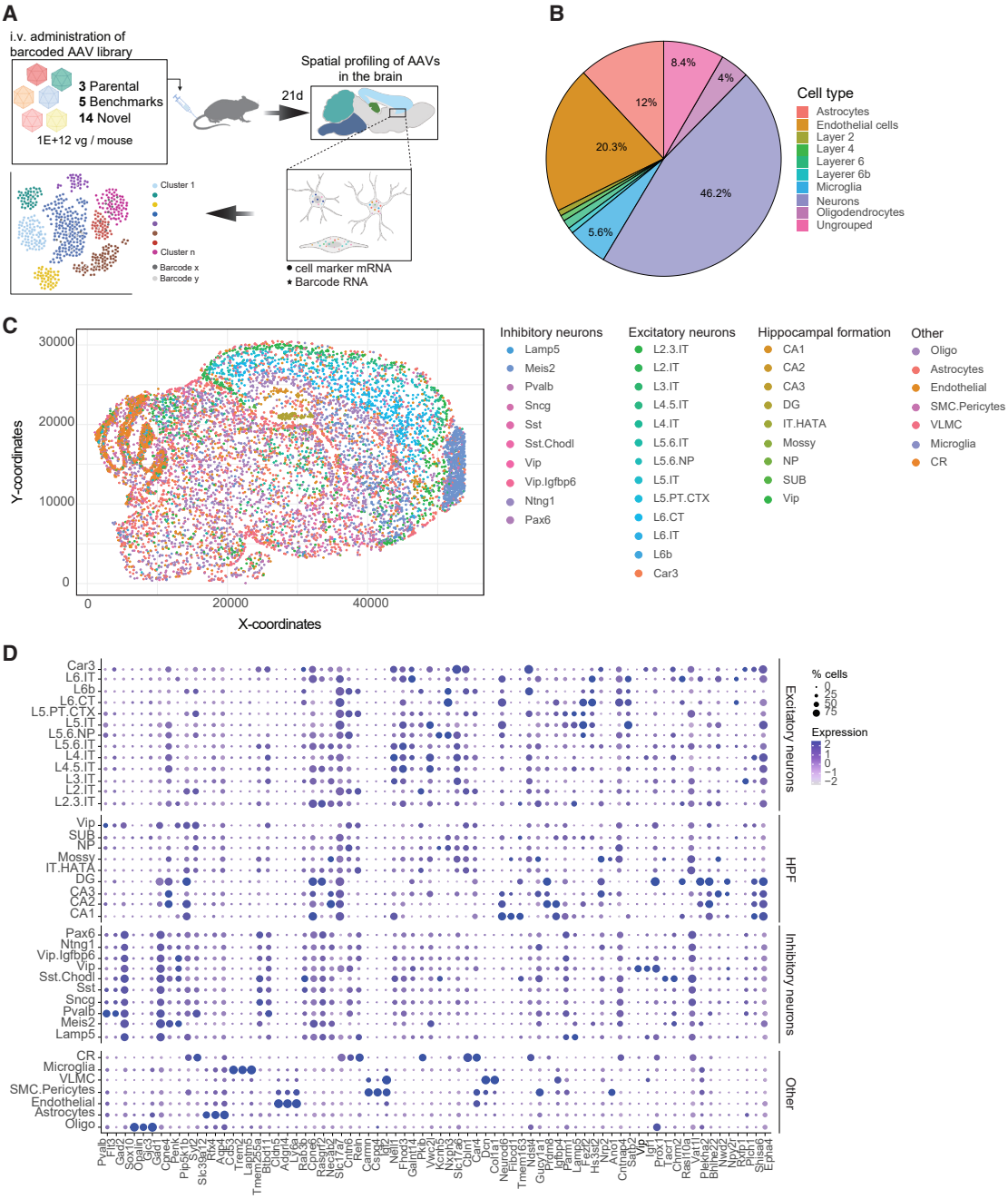

Figure 4. Clustering of neuronal and non-neuronal cell types using the 10× Genomics Xenium mouse brain gene expression panel

(A) Overview of the spatial transcriptomics *in vivo* experimental workflow. An AAV library consisting of 22 variants, each packaged with a GFP transgene fused to unique barcodes, packaged, was pooled and administered. Spatial tropism was quantified by *in situ* hybridization transcriptomics 21 days post-injection.

(B) Relative abundance of neuronal and non-neuronal cell types, as determined by endogenous cell marker mRNAs included in the 248-gene mouse brain expression panel. Each marker was detected using eight probes.

(C) Spatial map of clustered neuronal and non-neuronal cells from mouse brain. Each cluster is indicated by color. Cell type annotation and clustering were performed based on reference scRNA-seq data clusters and the Allen Brain Atlas.[40–42] The resulting clusters included 10 inhibitory neuron types, 13 excitatory neuron types, 9 hippocampal formation neuron types, and 7 non-neuronal cell types.

CR are cerebellar neurons potentially misannotated as Cajal-Retzius due to absence of cerebellar tissue in reference datasets.

(D) Heat maps display the marker genes used to define each cell cluster. Dot size represents the proportion of cells within a cluster expressing the marker gene, while color intensity reflects the expression level of that gene.

(legend continued on next page)

barcodes, likely because it was targeted by three probes, whereas each barcode was targeted by only a single probe.

Cumulative analysis of barcode-positive cell counts showed a strong correlation with bulk RNA-seq data (Figures 2C, 5C, and S6B). Approximately 25% of eGFP-positive cells were also positive for one or more barcodes, with a similar proportion observed for CMV promoter detection. This discrepancy could be due to differences in the abundance of viral DNA versus mRNA or differences in detection efficiency (Figure 5D). In contrast, ITR colocalization with eGFP was much lower (∼2%) (Figure 5D). Top-performing variants—including AAV9-BTX166, PHP.eB, CAP-B10, AAV-F, and AAV9P31—showed, on average, ∼37% of barcode-positive cells also expressing eGFP, confirming superior transduction and gene expression (Figure 5E). Conversely, lower-performing variants (AAV9-BTX003, -BTX002, -BTX063, -BTX001, AAV9, AAV9W 503R, and AAV2) showed ≤25% colocalization (Figure S6C), reflecting their reduced transcriptional capacities. CMV promoter and ITR elements showed even less colocalization with barcodes, likely due to lower probe efficiency and/or lower viral genome levels compared to viral mRNA (Figures 5E and S6C).

Benchmark vectors—including PHP.eB, CAP-B10, AAV9P31, AAV-F, and AAV-GNSSKQF—exhibited broad transduction and expression across the brain, with the cerebellum, cortex, and hindbrain containing the highest numbers of barcode-positive cells (Figures S7A and S7B). PHP.eB and CAP-B10 were each detected in over 4,000 cells, while AAV9P31 was detected in approximately 2,000 cells (Figure 5C). The novel candidates AAV9-BTX166 and -BTX168 were each found in ∼1,800 cells. In contrast, AAV2, AAV9, AAV9-BTX003, -BTX013, -BTX011, and -BTX024 were detected in fewer than 250 cells (Figures 5C and S7C) and, therefore, were excluded from further analysis to ensure robust interpretation.

Most of the novel AAV9 variants exhibited broad tropism across multiple brain regions (Figure S7D), with some exceptions. For example, the AAV9-BTX001 variant, engineered with the NRRPDDM peptide on the wild-type AAV9 capsid backbone, showed expression biased toward the striatum (Figures S7D–S7E). Interestingly, this pattern changes for its derivatives, AAV9-BTX149 and -BTX063, which incorporate the NRRPDDM and NRRPEDM peptides, respectively, into the AAV9W503R backbone, a modified platform with reduced hepatic tropism due to the W503R substitution. While AAV9-BTX149 (AAV9W503R-NRRPDDM) exhibited a scattered, low-intensity signal throughout the brain, AAV9-BTX063 (AAV9W503R-NRRPEDM) showed a concentrated signal localized specifically to the olfactory bulb (Figure S7E).

We further analyzed the cell-type specificity of barcoded AAV variants across neuronal and non-neuronal populations. Most AAVs preferentially transduced endothelial cells, with lower expression in SMC/pericytes and VLMCs (Figures 6A, S8A, and S8C). eGFP and CMV signals localized to vascular clusters, indicating limited BBB penetration for most variants (Figure 6A).

Among the novel candidates, AAV9-BTX166, -BTX168, -BTX173, and -BTX175 were top performers in bulk NGS (Figure 2C) and displayed enrichment in endothelial and pericyte/SMC clusters, depletion in VLMCs, oligodendrocytes, and microglia, and modest enrichment in astrocytes (Figures 6A, S8A, and S8F).

Further analysis of the PHP.eB capsid and its derivatives, CAP-B10 and AAV9-GNSSKQF,[18] revealed distinct cell-type tropism patterns consistent with previous reports. Both PHP.eB and CAP-B10 showed broad distribution across cell types and subcellular clusters but were depleted in oligodendrocytes, VLMCs, and microglia (Figures 6A, S8A, and S8F). Although less pronounced than previously described, PHP.eB exhibited a slightly stronger astrocyte bias than CAP-B10 (Figure 6A, enrichment; Figure S8E), consistent with prior comparisons between these two variants.[18,36] In the vascular compartment, PHP.eB and CAP-B10 were enriched in endothelial cells, showed minimal enrichment in SMC/pericyte subtypes, and were depleted in VLMCs (Figures S8A–S8C). GNSSKQF also showed an endothelial cells bias; nevertheless, it exhibited higher enrichment in SMC/pericyte clusters and less depletion in VLMCs than CAP-B10 or PHP.eB (Figure S8A–S8C).

PHP.eB and CAP-B10 displayed similar overall expression profiles in the brain (Figure 5E), and, similarly, pseudobulk analysis of glutamatergic and GABAergic neurons revealed comparable tropism of PHP.eB and CAP-B10 (Figures 6B–6E). In excitatory neurons, both were slightly depleted in L2/3, L6 (Slc17a7+/Tmem163), and L6b (Slc17a7/Tmem163) subtypes but variably enriched in L4 (Nell1/Shisa6), L5 (L5.IT, L5.6IT, L5.6.NP), and carbonic anhydrase 3 (Car3) clusters (Figures 6F, 6G, and S9A). In inhibitory neurons, both variants were enriched in Pvalb+ cells (Figure 6D), while depleted in Meis2+, Sst+, Vip+, Vip.insulin like growth factor binding protein 6 (Igfbp6+), and netrin G (Ntng1+) populations (Figures 6H and S9B). PHP.eB and CAP-B10 differed in lysosome-associated membrane glycoprotein 5 (Lamp5) cells, with PHP.eB modestly enriched and CAP-B10 depleted. In the hippocampal formation, both variants were depleted in mossy, dentate gyrus (DG), and intra-telencephalic (IT).hippocampo-amygdalar transition area (HATA) neurons. For hippocampal cornu ammonis area (CA) subtypes, PHP.eB was enriched in CA2 and especially

Lamp5, lysosome-associated membrane glycoprotein 5; Meis2, myeloid ecotropic viral integration site 1 homolog 2; Pvalb, parvalbumin; Sncg, synuclein gamma; Sst, somatostatin; Chodl, chondrolectin; Vip, vasoactive intestinal peptide; Igfbp6, insulin like growth factor binding protein 6; Ntng1, netrin G; Pax6, paired box 6; L, layer; IT, intra-telencephalic; NP, near-projecting; PT, pyramidal tract; CTX, cortex; CT, cortico-thalamic; Car3, carbonic anhydrase 3; HPF, hippocampal formation; CA, cornu ammonis area; DG, dentate gyrus; HATA, hippocampo-amygdalar transition area; SUB, subiculum; Oligo, oligodendrocytes; SMC/Pericytes, smooth muscle cells/pericytes; VLMCs, vascular leptomeningeal cells.

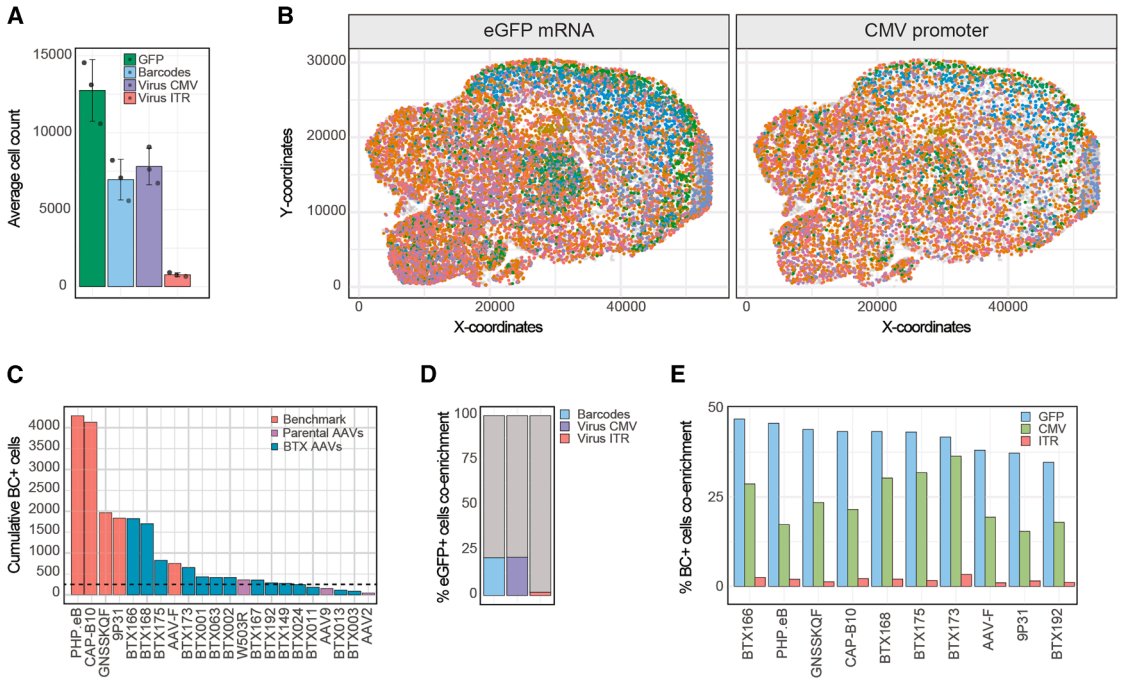

Figure 5. *In situ* detection of elements from a systemically delivered barcoded AAV capsid panel in the mouse brain

(A) Quantification of the average number of cells positive for eGFP, any barcode, viral-CMV, and ITR across three C57BL/6 mouse brains. Data are represented as mean ± SEM.

(B) *In situ* detection of eGFP-positive and viral-CMV-positive cells using padlock probes specific for each element. Each dot represents a positive cell, colored by cell subtype.

(C) Cumulative number of cells positive for each barcode across three mouse brain sections. The dashed line indicates the threshold of 250 positive cells per barcode required for further evaluation.

(D and E) Cumulative colocalization of eGFP mRNA/DNA with other viral elements, including the viral-CMV promoter, viral-ITR, and any barcode, as well as with (E) individual barcodes.

CA3, while CAP-B10 was enriched across all three CA regions (Figures 6I and 6J).[45]

AAV9P31 emerged as the most efficient variant from a peptide-displaying capsid library selected in C57BL/6 mice via RNA-driven biopanning.[13] Systemic administration of AAV9P31 yielded broad, homogeneous CNS transduction with distinct regional and cellular preferences.[13,46] In our analysis, AAV9P31 was detected across multiple brain regions (Figures S7A and S7B) and showed a non-neuronal tropism pattern similar to PHP.eB and CAP-B10 (Figure 6A). However, it was less enriched in endothelial and SMC/pericyte clusters (Figures S8A and S8B), depleted in oligodendrocytes and microglia, and displayed mild enrichment in astrocytes (Figures S8D–S8F). Notably, most AAVs tested lacked strong astrocyte enrichment; even the top variant, AAV-F, showed only modest astrocyte tropism (Figure S8E).

Within neuronal populations, AAV9P31 favored inhibitory neurons (Figures 6G and 6H), particularly paired box 6 (Pax6+), Sst.chondrolectin (Chodl+), and Pvalb+ subtypes, and uniquely drove expression in Vip+ inhibitory neurons, unlike PHP.eB and CAP-B10 (Figure S9B). Among excitatory cortical neurons, AAV9P31 was primarily enriched in L4.5.IT (Nell1/Cpne2), while showing depletion in L2/3, L6, and Car3 neurons (Figures 6G and S9A).

Among novel AAV9 variants, AAV9-BTX167 exhibited CNS eGFP expression comparable to parental AAV9 and AAV9W503R (Figures 2C and 5C). AAV9-BTX167 showed a neuronal bias, with modest enrichment in endothelial cells and pericytes (Figures 6A, S8A, and S8B), but was depleted in other non-neuronal cells (Figures S8C–S8F). It was enriched in excitatory neurons of layers 2/3, 4, 5, 6b, and Car3, as well as inhibitory subtypes including Lamp5, Vip+, and Pax6 clusters (Figures 6G, 6H, S9A, and S9B).

Despite lower overall transduction, AAV9-BTX063 and -BTX001 showed selective tropism toward inhibitory neurons. AAV9-BTX063 was enriched in Pax6+, Meis2+, and Vip.Igfbp6+ clusters (Figures 6G, 6H, S9A, and S9B) and depleted in non-neuronal cells (Figures 6A, S8A, and S8F). AAV9-BTX001 showed enrichment only in endothelial cells among non-neuronal populations (Figures 6A, S8A, and S8F) and was robustly detected in Meis2+ neurons, with lesser expression in Sst.Chodl+ and Vip.Igfbp6+ cells, localized to a specific brain region across two samples (Figures S7E, S9B).

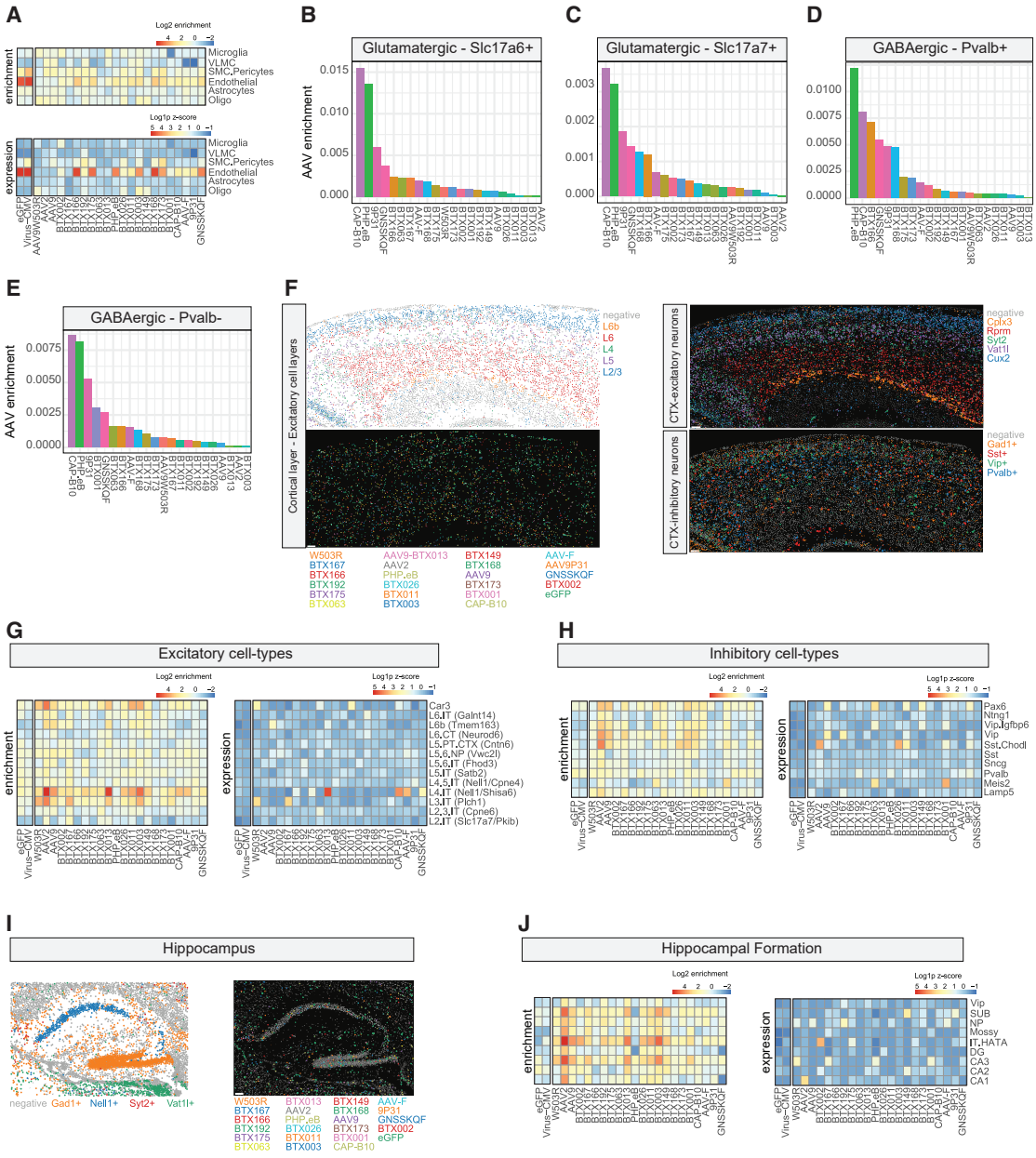

Figure 6. Neuronal and non-neuronal subtype tropism of systemically delivered barcoded AAVs in C57BL/6 mouse brain

(A–E) Relative enrichment and z-scored expression of AAV barcodes in non-neuronal cell type clusters. AAV gene expression was also assessed in major neuronal cell types, including (B) glutamatergic Slc17a6+ neurons, (C) glutamatergic Slc17a7+ neurons, (D) GABAergic Pvalb+ neurons, and (E) GABAergic Pvalb-neurons.

(F–H) Representative image showing: organization of excitatory cell layers in the cortex (top left; L6b, L6, L5, L4, L2/3), distribution of all 22 AAV variants and eGFP (lower left), markers of cortical excitatory cells (top right; Cplx3, Rprm, Syt2, Vat1l, Cux2), and markers for inhibitory cells within cortical layers (lower right; Gad1+, Sst+, Vip+, Pvalb+). Scale bars, 100 μm. Relative enrichment and *Z* scored expression of AAVs in (G) excitatory and (H) inhibitory neuronal cell types. For excitatory neurons, top expressed cell markers are indicated.

(I) Representative image showing cell types in the hippocampus (left; Gad1, Nell1, Syt2, Vat1l) and the distribution of all 22 AAV variants and eGFP (right). Scale bars, 100 μm.

(J) Relative enrichment and *Z* scored expression of AAV cargo in the hippocampal formation.

DISCUSSION

Historically, functional screening of AAV libraries has focused on engineering capsid variants to enhance CNS tropism and minimize off-target transduction—especially in the liver—typically benchmarking new variants against parental serotypes for their ability to cross the BBB and drive widespread transgene expression in rodent

and, increasingly, NHP models.[13,40,46,47] More recently, however, advances in screening approaches and analytics have enabled assessments at cellular resolution, providing a more comprehensive characterization of capsid performance beyond what traditional single-vector biodistribution studies can offer amid the rapid pace of capsid development. While bulk tissue assays lack the resolution to detect subtle differences in cell-type or regional targeting, scRNA-seq—though powerful—does not preserve the spatial context needed to fully understand gene delivery in complex tissues like the brain.[30,31]

Recent advances in spatial transcriptomics are bridging critical gaps in AAV vector characterization by enabling single-cell resolution mapping of gene expression and viral transduction within intact tissue architecture. These technologies not only identify transduced cell types but also reveal their precise anatomical locations—information essential for both basic neuroscience and translational gene therapy applications. Innovations such as USeqFISH,[36] combined with high-throughput barcoded AAV libraries, have demonstrated the value of multiplexed, *in situ* profiling for efficient vector screening and optimization.

In this study, iterative *in vivo* screening of AAV9 peptide display libraries in C57BL/6 mice identified several novel capsid variants with markedly enhanced brain tropism and reduced liver targeting, outperforming both parental AAV9 and AAV9W503R.[20] Notably, variants such as AAV9-BTX002, -BTX166, -BTX168, -BTX173, and -BTX175 demonstrated robust CNS transduction, with AAV9-BTX166 achieving CNS enrichment comparable to AAV9P31 and surpassing established vectors such as PHP.eB and CAP-B10. Additional variants, including AAV9-BTX167 and -BTX192, outperformed AAV9 in brain transduction; however, only AAV9-BTX002, -BTX166, -BTX175, -BTX173, and -BTX168 achieved significantly higher cargo transcription than AAV9, suggesting that post-entry or transcriptional barriers may limit the efficacy of other novel variants. Alternatively, the less efficient novel variants may achieve higher specificity by targeting a narrower range of cell types in the brain, a feature of variants such as AAV9-BTX001 (discussed below). Importantly, while PHP.eB and CAP-B10 depend on the Ly6A receptor to cross the BBB and lose efficacy in BALB/c mice,[38,39] three novel variants—AAV9-BTX002, -BTX168, and -BTX173—maintained CNS transduction across mouse strains, suggesting distinct mechanisms of cell entry and receptor usage. A recent report on novel AAV9 variants, AAV9-Se1 and AAV9-Se2,[20] demonstrates enhanced brain targeting accompanied by reduced liver tropism in both mouse and marmoset models. Importantly, AAV9-Se2 was found to primarily engage Ly6C1, a homologue of the Ly6A receptor, indicating an alternative and potentially evolutionarily conserved pathway for crossing the BBB. This shift in receptor usage highlights the critical role of exploring new cellular entry mechanisms to achieve efficient and selective CNS gene delivery, particularly for translational applications. However, the exact pathways enabling CNS transduction by all the novel variants, and specifically, AAV9-BTX002, -BTX168, and -BTX173, remain to be elucidated and characterized in follow-up mechanistic studies.

Validation of the 10× Genomics Xenium spatial *in situ* hybridization platform confirmed that single barcode-targeting padlock probes enable differential and specific profiling of barcoded AAV cargo transcripts. This multiplexed detection, combined with endogenous cell-type markers, allowed precise quantification of transduction efficiency and cell-type specificity in pooled experiments. Spatial transcriptomics data showed a strong correlation between barcode-positive cell counts and bulk RNA-seq results in C57BL/6 mice, independently validating the efficiency of single-probe AAV detection.

However, detection efficiency was strongly influenced by the number of probes per target. eGFP, targeted by three probes, was detected more consistently than barcodes, which were targeted by a single probe. This difference likely accounts for the limited overlap between eGFP-positive and barcode-positive cells, despite both being part of the same mRNA. Since the reporter gene and the barcode are co-expressed, these detection discrepancies reflect technical limitations rather than biological differences. Specifically, the lower number of probes targeting the barcode likely reduced detection sensitivity, leading to an underestimation of barcode-positive cells.

These findings underscore the importance of probe design and optimization in spatial transcriptomics. Increasing the number of probes per barcode, as shown in recent approaches such as USeqFISH,[36] could enhance detection sensitivity and improve cell labeling accuracy, making probe set optimization essential for generating reliable and interpretable data.

Our cell-type annotation strategy, which incorporated 248 marker genes, multiple reference datasets, and the Allen Brain Atlas,[41–43] enabled the identification of 39 distinct clusters encompassing diverse neuronal and non-neuronal cell types, including astrocytes, oligodendrocytes, and endothelial cells. This comprehensive framework allowed us to dissect AAV tropism at single-cell resolution. Systematic mapping of viral transgene expression across these populations revealed nuanced, and sometimes unexpected, patterns of cell-type specificity, highlighting the critical role of spatial context in evaluating viral vector performance.

In vivo spatial data showed that eGFP and CMV signals were predominantly localized within vascular clusters, indicating that many AAV variants preferentially target endothelial cells and, to a lesser extent, other vascular cell types. This highlights the ongoing challenge of achieving efficient BBB traversal with systemically delivered vectors, which limits access to parenchymal cell types in the CNS. Novel variants AAV9-BTX166 and -BTX168 exemplify this pattern, displaying strong selectivity for endothelial and pericyte/SMC clusters while being depleted in other non-neuronal and neuronal populations—insights not apparent from their relative enrichment compared to parental AAV9 in bulk analytics alone. These findings further demonstrate the utility of *in situ* hybridization transcriptomics for accurately mapping the spatial distribution of AAV variants.

Further validating the spatial transcriptomics approach, our study confirmed several, though not all, previously reported features of benchmark vectors PHP.eB and CAP-B10. PHP.eB exhibited a slight tropism bias toward astrocytes compared to its derivative CAP-B10, while CAP-B10 showed a modestly higher preference for glutamatergic excitatory neurons. In inhibitory neurons, both vectors were most enriched in Pvalb+ subtypes and were non-enriched or depleted in other inhibitory clusters. Some deviations from prior studies may be due to differences in cell cluster annotation. We also observed enrichment of PHP.eB, and to a lesser extent CAP-B10, in endothelial cells—a pattern seen with other benchmarks such as AAV-F and AAV9P31, though to varying degrees. The discrepancy from previous reports[36] may be explained by the tendency of USeqFISH to underestimate non-neuronal cells, whereas our computational cell segmentation likely provides more accurate cell boundaries.

Moreover, the modest astrocyte enrichment observed for PHP.eB and CAP-B10,[11,24,26,36,48,49] relative to their reported tropism in prior studies was a universal observation across all tested variants and could potentially be explained by two factors. First, we used CMV to drive barcoded eGFP expression, unlike the cytomegalovirus early enhancer/chicken β-actin (CAG) or cell type–specific promoters used in the reference studies, as CMV shows reduced efficiency in astrocytes of rats and mice.[50] Second, our 22-AAV library contrasts with pooled or single-variant tests, in which capsid context can influences neuron-versus-astrocyte ratios.[11,24,26,36,48]

Importantly, we identified two novel variants, AAV9-BTX149 and AAV9-BTX001, both carrying the NRRPDDM peptide insert but on different parental backbones: BTX149 on liver-detargeted AAV9-W503R and BTX001 on wild-type AAV9. Despite sharing the same peptide, these variants exhibited distinct tropism profiles. AAV9-BTX149 exhibited a scattered, low-intensity signal throughout the brain, possibly due to subthreshold transgene expression or limitations in probe detection sensitivity. In contrast, BTX001, although low in bulk RNA-seq and spatial transcriptomics, displayed specific tropism for Meis2+ inhibitory neurons. A third related variant, carrying the NRRPEDM peptide on an AAV9W503R backbone, also showed reduced overall expression but was enriched in Meis2+, Pax6+, Vip.Igfbp6+, and Sst.Chodl+ inhibitory clusters. Notably, AAV9-BTX063 exhibited spatially restricted signal in the olfactory bulb. These findings suggest that low expression in bulk assays may indicate highly specific tropism for rare cell types, rather than inefficient transduction. This challenges conventional directed evolution strategies that prioritize candidates with high overall abundance and highlights the need to include moderately abundant variants in validation pipelines to capture cell-type-specific targeting.

The marked differences in tropism observed among AAV9-BTX001, -BTX063, and -BTX149 illustrate how single amino acid substitutions or alterations in the parental capsid backbone can profoundly influence vector specificity. For instance, replacing wild-type AAV9 in AAV9-BTX001 with the AAV9W503R backbone in AAV9-BTX149 shifted its tropism from predominantly neuron-specific to a more diffuse, vascular, and pan-cellular pattern. These observations parallel recent findings by Gianelli et al., who demonstrated that AAV-A503-Se1/2 variants lacking galactose binding exhibited highly selective transduction of brain endothelial cells in both C57BL/6 and BALB/c mouse strains, with limited infection of non-endothelial cells. Restoration of galactose binding via W503 reconstitution, particularly in AAV-Se2, significantly enhanced neuronal and glial transduction throughout the brain.[20] Likewise, previous studies have shown that a single Q587N mutation can redirect tropism from vascular to neuronal populations in mice.[19,51–53] Notably, even variants with robust inter-strain CNS tropism, such as AAV9-BTX002, -BTX168, and -BTX173, showed predominant endothelial targeting in spatial analyses. These results underscore the need for iterative engineering to enhance BBB traversal in endothelial-focused variants, while further detargeting the liver in neuron-specific candidates such as BTX001 and BTX063.

While our findings advance AAV vector engineering and characterization, several limitations remain. First, mouse models, though informative, may not fully recapitulate human CNS biology or immune responses. Future studies should extend this approach to NHPs and, where possible, human tissue models to validate cell-type tropism, particularly for promising candidates such as AAV9-BTX001. Second, our spatial transcriptomics panel covered a wide range of cell types, but some region-specific populations, such as cerebellar neurons annotated as CR, may be incompletely or inaccurately assigned due to reference dataset limitations. Refining cell-type annotation, expanding marker panels, and integrating scRNA-seq could further improve resolution and clustering accuracy.

Barcode-based multiplexing enables robust comparative analysis of AAV variants in pooled experiments, but potential interactions or competition among co-administered vectors should be considered. Although we profiled 22 variants simultaneously, future work could refine these findings by testing smaller subgroups or individual candidates in isolation to distinguish intrinsic capsid properties from context-dependent effects. Additionally, combining capsid engineering with cell-type-specific promoters or regulatory elements may help isolate tropism effects from transcriptional biases. Further mechanistic and functional studies, including those investigating AAV9-BTX001 selective Meis2+ inhibitory neuron targeting or AAV9-BTX063 olfactory bulb specificity, will be essential to fully resolve vector biology.

In summary, our comprehensive evaluation of a barcoded AAV library in the mouse brain demonstrates the feasibility and power of combining high-throughput *in vivo* screening, bulk sequencing, and spatial transcriptomics for the discovery and characterization of CNS-targeted gene therapy vectors. Integrating spatially resolved molecular profiling will be instrumental in designing and selecting next-generation AAV vectors with precise tissue- and cell-type-targeting capabilities.

Limitations and future perspectives

Our study demonstrates the transformative potential of the Xenium platform for high-resolution AAV tropism profiling, yet refinements are needed for translational impact. Single-probe targeting of 15-nt barcodes enabled robust multiplexing of 22 variants with detailed cell-type mapping, though detection efficiency varied, ranging from ∼56% for BC30 to >80% for most variants, likely due to sequence-specific accessibility. Detecting eGFP with 3 probes and CMV with 7 probes showed systematically higher detection than single-probe barcodes despite co-expression on the same cassette, with count discrepancies reflecting technical differences in probe number rather than biological variation. Future designs adopting longer barcodes with multiple padlock probes per variant, as in USeqFISH,[36] will harmonize sensitivity across targets barcodes with eGFP, enhance low-abundance transcript detection, and reduce under-detection biases for rare cell types.

Systemic administration AAVs encapsulating barcoded CMV-driven eGFP cargo resulted in ∼2.5% transduced cells. This pattern underscores the challenge of achieving efficient BBB traversal and parenchymal expression with intravenous (i.v.) delivery and potential limitations of CMV promoter-driven expression. Future studies should incorporate enhancer elements and/or use stronger promoters, such as CAG, as well as employ alternative routes of administration to boost the widespread of expression of the cargo and potentially reveal tropism currently masked by transcriptional barriers.

While pooled barcoded library screening offers an efficient, high-throughput strategy to compare 22 AAV variants within intact tissue, future studies are necessary to resolve intrinsic capsid properties and confirm cell-type and subcellular tropism not only in mice but also by extending the approach to other strains and species, including NHPs. At present, no commercial Xenium panels were available for NHP brain, necessitating the development and testing of custom marker panels—a labor-intensive barrier to cross-species validation. Extending this approach to NHPs and/or human induced pluripotent stem cell (iPSC)-derived organoids,[54,55] paired with expanded reference atlases, will be essential for assessing translational relevance, enabling the targeting of rare, pathology-specific cell types in heterogeneous brain regions. Finally, spatial mRNA data cannot confirm protein expression, cell viability, or therapeutic cargo performance. Integrating spatial transcriptomics with complementary modalities, such as scRNA-seq, spatial proteomics, and pathology models, will be crucial for translating these findings into clinically actionable strategies.

METHODS

AAV peptide display libraries and constructs generation

Plasmids for AAV peptide display library construction were generated by cloning AAV2 Rep and either AAV9 Cap or AAV9W503R Cap genes into an ITR-containing plasmid backbone. Unique SfiI restriction sites were engineered flanking the designated insertion site within the AAV Cap gene to facilitate peptide insertion. Oligonucleotides encoding random 7-mer and 12-mer peptides ($[NNK]_{]}$ and $[NNK]_{12}$ libraries) were synthesized and cloned by Geneart in loop VIII at position ($Q_{588}A_{589}G_{590}(NNK)_{7/12}A_{591}Q_{592}A_{593}$) (Thermo Fisher Scientific, Germany). The pooled plasmid libraries were transformed into ElectroMAX DH5α-E Competent Cells (Thermo Fisher Scientific, Germany), and plasmid DNA was isolated using the Qiagen Maxi Prep Endofree Kit (QIAGEN, Germany).

For secondary library rounds, viral genomic DNA was extracted from brain lysates using the QIAamp DNA Mini Kit (QIAGEN, Germany). The variable regions of the AAV library were amplified with serotype-specific primers and Phusion High-Fidelity DNA Polymerase (Thermo Fisher Scientific, Germany), then subcloned into recipient plasmids and retransformed into ElectroMAX DH5α-E cells.

To produce barcoded recombinant AAV, a CMV-driven eGFP reporter cassette containing a 15-nucleotide barcode sequence in the 3′ UTR, as described previously,[28] and flanked by AAV2 ITRs, was utilized.

AAV production

AAV production and titration were performed as described previously.[56] AAVs were produced in HEK293H cells (acCELLerate, Germany) via triple transfection using calcium phosphate precipitation. For each variant, three 8-layer CELLdiscs (Greiner Bio-One, Austria) were seeded with 1.5×10^4 cells/cm^2 3 days prior to transfection. Transfection utilized three plasmids: the barcoded-eGFP reporter, a rep/cap plasmid (parental or recombinant), and the adenoviral helper plasmid. After 6 h, the transfection medium was replaced with fresh DMEM, and cells were incubated for 3 days before harvest.

Cells were detached with EDTA, pelleted, and resuspended in lysis buffer (1 M NaCl, 50 mM Tris, 20 mM $MgCl_2$, 0.001% Pluronic F-68, pH 8.5). Lysis was achieved by two freeze/thaw cycles, followed by digestion with salt-active nuclease (ArcticZymes Technologies, Norway) to degrade nucleic acids. AAV particles were precipitated with polyethylene glycol (PEG; Sigma-Aldrich, Germany) and resuspended overnight.

Viral purification was performed using stepwise iodixanol gradients (15%, 25%, 40%, 54%) and ultracentrifugation in a Type 70 Ti rotor at 69,100 rpm for 1 h and 9 min. The AAV-containing iodixanol fraction was concentrated and buffer-exchanged into formulation buffer (1× PBS, pH 7.4, 1 mM $MgCl_2$, 2.5 mM KCl, 10% glycol, 0.001% Pluronic F-68) using 100 kDa Amicon-15 tubes (Merck Millipore, Germany).

Animals

All procedures involving animals were reviewed and approved by the regional authority (Tübingen, Germany, application number: 20-021-G) and performed in compliance with Directive 2010/63/EU governing the use of animals in scientific research. Upon arrival, mice were housed in a controlled environment with a 12-h light/dark cycle and unrestricted access to food and water. Animals

were given at least 1 week to acclimate before experimental procedures began.

For systemic delivery of barcoded AAV vector libraries, 10-12-weeks-old female C57BL/6NCrl or BALB/c mice (Charles River, Germany) were injected systemically via the tail vein with 1E+11 – 1E+12 vg suspended in 100 µL of solution. After a period of 3 weeks, animals were euthanized, and tissues were collected for downstream analyses.

Extraction of DNA and RNA

AAV genomes were extracted using the ViralXpress DNA/RNA extraction reagent (Sigma-Aldrich, Germany) according to the manufacturer's instructions. For tissue nucleic acid extraction, 30 mg of mouse tissue was homogenized in RLT buffer, and DNA and RNA were isolated using the Allprep DNA/RNA Mini Kit (Qiagen, Germany) following the manufacturer's protocol. RNA samples were treated with DNase I (Qiagen, Germany) prior to cDNA synthesis, which was performed using the Maxima H Minus cDNA Synthesis Master Mix with dsDNase (Thermo Fisher Scientific, Germany).

DNA and RNA NGS

RNA was reverse-transcribed to cDNA using the Maxima H Minus cDNA Synthesis Master Mix with dsDNase (Thermo Fisher Scientific, Germany). Barcoded nucleic acids from both DNA and cDNA samples were amplified for 30 cycles using Phusion DNA Polymerase (Thermo Fisher Scientific, Germany) and staggered primers with Illumina TruSeq overhangs. Amplicons were purified with Agencourt AMPure XP beads (Merck) and quality-checked using the Agilent NGS kit (Agilent). Each sample was then multiplexed using NEBNext Ultra II Q5 Master Mix and UDI index primers (New England Biolabs).

Following further purification and quantification, libraries were pooled, denatured, spiked with PhiX, and sequenced on an Illumina NovaSeq6000. Sequencing reads were demultiplexed using UDI indices. AAV composition in each sample was normalized to the injected pool, and RNA abundance and vector distribution were calculated by multiplying the AAV composition by the DNA/RNA levels from the entire pool.

Xenium experiment

In situ spatial transcriptomic profiling was performed on 5 µm FFPE sagittal brain sections from three barcoded-AAV library-treated C57BL/6 mice using the 10× Genomics Xenium platform (protocol CG000582 Rev E). The predesigned 248-gene Mouse Brain Gene Expression panel was supplemented with custom probes targeting AAV barcodes, the CMV promoter, eGFP, and ITRs. Tissue sections were mounted on Xenium slides, dried, and deparaffinized through sequential xylene and ethanol incubations. Following decrosslinking, sections were washed and subjected to overnight probe hybridization, followed by ligation and rolling circle amplification. Background fluorescence was chemically quenched prior to imaging. Imaging and signal decoding were performed on the Xenium Analyzer, and data were processed using QPath and Xenium Explorer software.

Cell type assignment, expression profiling, and plotting

Cell types were assigned based on the cell type-specific gene expression profiles provided by the Allen Brain Institute (ABI) for the mouse brain isocortex and hippocampus.[41] The profile based on trimmed mean gene expression counts per cell type was used, filtering for the 298 genes in the Xenium panel. Cell type assignment was performed using the SingleR R package (version 2.6.0), applying this reference to the cells and gene counts identified by the Xenium pipeline. Cell types were mapped to the original ABI fine-grained cell types and manually grouped into broader categories. Gene expression profiles per cell type were calculated by taking the mean count across cells assigned to that type. Log1p expression values were calculated by adding a pseudocount of 1 to the mean gene counts and taking the natural logarithm. Log2 enrichment was calculated by taking the log2 of the observed proportion of cells of a given type expressing the barcode divided by the expected proportion (the proportion of that cell type in the total), whereby a pseudocount of 1 cell was added per cell type. The Seurat V5 R package was used for gene expression dot plots.[57] Spatial coordinate plots were created using Xenium Explorer, as well as the ggplot2 R package (version 3.5.1), with cell X and Y coordinates from the Xenium pipeline. For the R spatial coordinate plots, the data were downsampled to 10,000 cells to make plotting computationally feasible. Heatmaps were created using the pheatmap R package (version 1.0.12).

DATA AND CODE AVAILABILITY

The supporting data of this study can be obtained from the corresponding author upon reasonable request.

ACKNOWLEDGMENTS

The authors extend their gratitude to Phillipp Doll, Isabel Lang, Gudrun Zimmermann, Christine Mayer, Nadine Rehm, and Martina Steinrock for their valuable technical assistance and scientific insights. This study was funded by Eye Health & Research Beyond Borders (EH&RBB), Boehringer Ingelheim Pharma GmbH & Co. KG, Biberach (Riss), Germany, and supported by the Boehringer Ingelheim Discovery Research Postdoc program. The graphics and the graphical abstract was generated using biorender.com.

AUTHOR CONTRIBUTIONS

Conceptualization, Y.F., D.B., S.J., J.D., and S.M.; investigation, Y.F., D.B., M.J.D., S.K., S.A., T.S., W.R.; data curation, M.O. and G.A.-L.; formal analysis, Y.F.; M.O., S.J., D.B., S.K., J.D., S.M.; writing-original draft, Y.F. and S.M. All authors contributed to reviewing and editing the manuscript.

DECLARATION OF INTERESTS

All authors report a relationship with Boehringer Ingelheim Pharma GmbH & Co. KG that includes employment.

SUPPLEMENTAL INFORMATION

Supplemental information can be found online at https://doi.org/10.1016/j.omta.2026.201693.

REFERENCES

1. Bedbrook, C.N., Deverman, B.E., and Gradinaru, V. (2018). Viral Strategies for Targeting the Central and Peripheral Nervous Systems. Annu. Rev. Neurosci. *41*, 323–348. https://doi.org/10.1146/annurev-neuro-080317-062048.

2. Haery, L., Deverman, B.E., Matho, K.S., Cetin, A., Woodard, K., Cepko, C., Guerin, K.I., Rego, M.A., Ersing, I., Bachle, S.M., et al. (2019). Adeno-Associated Virus Technologies and Methods for Targeted Neuronal Manipulation. Front. Neuroanat. *13*, 93. https://doi.org/10.3389/fnana.2019.00093.

3. Martier, R., and Konstantinova, P. (2020). Gene Therapy for Neurodegenerative Diseases: Slowing Down the Ticking Clock. Front. Neurosci. *14*, 580179. https://doi.org/10.3389/fnins.2020.580179.

4. Kantor, B., O'Donovan, B., and Chiba-Falek, O. (2025). Trends and challenges of AAV-delivered gene editing therapeutics for CNS disorders: Implications for neurodegenerative disease. Mol. Ther. Nucleic Acids *36*, 102635. https://doi.org/10.1016/j.omtn.2025.102635.

5. Kishimoto, T.K., and Samulski, R.J. (2022). Addressing high dose AAV toxicity – 'one and done' or 'slower and lower. Expert Opin. Biol. Ther. *22*, 1067–1071. https://doi.org/10.1080/14712598.2022.2060737.

6. Lopez-Gordo, E., Chamberlain, K., Riyad, J.M., Kohlbrenner, E., and Weber, T. (2024). Natural Adeno-Associated Virus Serotypes and Engineered Adeno-Associated Virus Capsid Variants: Tropism Differences and Mechanistic Insights. Viruses *16*, 442. https://doi.org/10.3390/v16030442.

7. McCown, T.J. (2011). Adeno-Associated Virus (AAV) Vectors in the CNS. Curr. Gene Ther. *11*, 181–188. https://doi.org/10.2174/156652311795684759.

8. Macdonald, J., Marx, J., and Büning, H. (2021). Capsid-Engineering for Central Nervous System-Directed Gene Therapy with Adeno-Associated Virus Vectors. Hum. Gene Ther. *32*, 1096–1119. https://doi.org/10.1089/hum.2021.169.

9. Nisanov, A.M., Rivera de Jesús, J.A., and Schaffer, D.V. (2025). Advances in AAV capsid engineering: Integrating rational design, directed evolution and machine learning. Mol. Ther. *33*, 1937–1945. https://doi.org/10.1016/j.ymthe.2025.03.056.

10. Szumska, J., and Grimm, D. (2023). Boosters for adeno-associated virus (AAV) vector (r)evolution. Cytotherapy *25*, 254–260. https://doi.org/10.1016/j.jcyt.2022.07.005.

11. Deverman, B.E., Pravdo, P.L., Simpson, B.P., Kumar, S.R., Chan, K.Y., Banerjee, A., Wu, W.-L., Yang, B., Huber, N., Pasca, S.P., et al. (2016). Cre-dependent selection yields AAV variants for widespread gene transfer to the adult brain. Nat. Biotechnol. *34*, 204–209. https://doi.org/10.1038/nbt.3440.

12. Ravindra Kumar, S., Miles, T.F., Chen, X., Brown, D., Dobreva, T., Huang, Q., Ding, X., Luo, Y., Einarsson, P.H., Greenbaum, A., et al. (2020). Multiplexed Cre-dependent selection yields systemic AAVs for targeting distinct brain cell types. Nat. Methods *17*, 541–550. https://doi.org/10.1038/s41592-020-0799-7.

13. Nonnenmacher, M., Wang, W., Child, M.A., Ren, X.-Q., Huang, C., Ren, A.Z., Tocci, J., Chen, Q., Bittner, K., Tyson, K., et al. (2021). Rapid evolution of blood-brain-barrier-penetrating AAV capsids by RNA-driven biopanning. Mol. Ther. Methods Clin. Dev. *20*, 366–378. https://doi.org/10.1016/j.omtm.2020.12.006.

14. Hanlon, K.S., Meltzer, J.C., Buzhdygan, T., Cheng, M.J., Sena-Esteves, M., Bennett, R.E., Sullivan, T.P., Razmpour, R., Gong, Y., Ng, C., et al. (2019). Selection of an Efficient AAV Vector for Robust CNS Transgene Expression. Mol. Ther. Methods Clin. Dev. *15*, 320–332. https://doi.org/10.1016/j.omtm.2019.10.007.

15. Davidsson, M., Wang, G., Aldrin-Kirk, P., Cardoso, T., Nolbrant, S., Hartnor, M., Mudannayake, J., Parmar, M., and Björklund, T. (2019). A systematic capsid evolution approach performed in vivo for the design of AAV vectors with tailored properties and tropism. Proc. Natl. Acad. Sci. *116*, 27053–27062. https://doi.org/10.1073/pnas.1910061116.

16. Müller, O.J., Kaul, F., Weitzman, M.D., Pasqualini, R., Arap, W., Kleinschmidt, J.A., and Trepel, M. (2003). Random peptide libraries displayed on adeno-associated virus to select for targeted gene therapy vectors. Nat. Biotechnol. *21*, 1040–1046. https://doi.org/10.1038/nbt856.

17. Perabo, L., Büning, H., Kofler, D.M., Ried, M.U., Girod, A., Wendtner, C.M., Enssle, J., and Hallek, M. (2003). In vitro selection of viral vectors with modified tropism: the adeno-associated virus display. Mol. Ther. *8*, 151–157. https://doi.org/10.1016/s1525-0016(03)00123-0.

18. Goertsen, D., Flytzanis, N.C., Goeden, N., Chuapoco, M.R., Cummins, A., Chen, Y., Fan, Y., Zhang, Q., Sharma, J., Duan, Y., et al. (2022). AAV capsid variants with brain-wide transgene expression and decreased liver targeting after intravenous delivery in mouse and marmoset. Nat. Neurosci. *25*, 106–115. https://doi.org/10.1038/s41593-021-00969-4.

19. Körbelin, J., Dogbevia, G., Michelfelder, S., Ridder, D.A., Hunger, A., Wenzel, J., Seismann, H., Lampe, M., Bannach, J., Pasparakis, M., et al. (2016). A brain microvasculature endothelial cell-specific viral vector with the potential to treat neurovascular and neurological diseases. EMBO Mol. Med. *8*, 609–625. https://doi.org/10.15252/emmm.201506078.

20. Giannelli, S.G., Luoni, M., Iannielli, A., Middeldorp, J., Philippens, I., Bido, S., Körbelin, J., and Broccoli, V. (2024). New AAV9 engineered variants with enhanced neurotropism and reduced liver off-targeting in mice and marmosets. iScience *27*, 109777. https://doi.org/10.1016/j.isci.2024.109777.

21. Körbelin, J., Sieber, T., Michelfelder, S., Lunding, L., Spies, E., Hunger, A., Alawi, M., Rapti, K., Indenbirken, D., Müller, O.J., et al. (2016). Pulmonary Targeting of Adeno-associated Viral Vectors by Next-generation Sequencing-guided Screening of Random Capsid Displayed Peptide Libraries. Mol. Ther. *24*, 1050–1061. https://doi.org/10.1038/mt.2016.62.

22. Tabebordbar, M., Lagerborg, K.A., Stanton, A., King, E.M., Ye, S., Tellez, L., Krunnfusz, A., Tavakoli, S., Widrick, J.J., Messemer, K.A., et al. (2021). Directed evolution of a family of AAV capsid variants enabling potent muscle-directed gene delivery across species. Cell *184*, 4919–4938.e22. https://doi.org/10.1016/j.cell.2021.08.028.

23. Hordeaux, J., Buza, E.L., Dyer, C., Goode, T., Mitchell, T.W., Richman, L., Denton, N., Hinderer, C., Katz, N., Schmid, R., et al. (2020). Adeno-Associated Virus-Induced Dorsal Root Ganglion Pathology. Hum. Gene Ther. *31*, 808–818. https://doi.org/10.1089/hum.2020.167.

24. Chan, K.Y., Jang, M.J., Yoo, B.B., Greenbaum, A., Ravi, N., Wu, W.-L., Sánchez-Guardado, L., Lois, C., Mazmanian, S.K., Deverman, B.E., et al. (2017). Engineered AAVs for efficient noninvasive gene delivery to the central and peripheral nervous systems. Nat. Neurosci. *20*, 1172–1179. https://doi.org/10.1038/nn.4593.

25. Tordo, J., O'Leary, C., Antunes, A.S.L.M., Palomar, N., Aldrin-Kirk, P., Basche, M., Bennett, A., D'Souza, Z., Gleitz, H., Godwin, A., et al. (2018). A novel adeno-associated virus capsid with enhanced neurotropism corrects a lysosomal transmembrane enzyme deficiency. Brain *141*, 2014–2031. https://doi.org/10.1093/brain/awy126.

26. Matsuzaki, Y., Konno, A., Mochizuki, R., Shinohara, Y., Nitta, K., Okada, Y., and Hirai, H. (2018). Intravenous administration of the adeno-associated virus-PHP.B capsid fails to upregulate transduction efficiency in the marmoset brain. Neurosci. Lett. *665*, 182–188. https://doi.org/10.1016/j.neulet.2017.11.049.

27. Hordeaux, J., Wang, Q., Katz, N., Buza, E.L., Bell, P., and Wilson, J.M. (2018). The Neurotropic Properties of AAV-PHP.B Are Limited to C57BL/6J Mice. Mol. Ther. *26*, 664–668. https://doi.org/10.1016/j.ymthe.2018.01.018.

28. Weinmann, J., Weis, S., Sippel, J., Tulalamba, W., Remes, A., El Andari, J., Herrmann, A.-K., Pham, Q.H., Borowski, C., Hille, S., et al. (2020). Identification of a myotropic AAV by massively parallel in vivo evaluation of barcoded capsid variants. Nat. Commun. *11*, 5432. https://doi.org/10.1038/s41467-020-19230-w.

29. Xu, M., Li, J., Xie, J., He, R., Su, Q., Gao, G., and Tai, P.W.L. (2019). High-Throughput Quantification of In Vivo Adeno-Associated Virus Transduction with Barcoded Non-Coding RNAs. Hum. Gene Ther. *30*, 946–956. https://doi.org/10.1089/hum.2018.253.

30. Brown, D., Altermatt, M., Dobreva, T., Chen, S., Wang, A., Thomson, M., and Gradinaru, V. (2021). Deep Parallel Characterization of AAV Tropism and AAV-Mediated Transcriptional Changes via Single-Cell RNA Sequencing. Front. Immunol. *12*, 730825. https://doi.org/10.3389/fimmu.2021.730825.

31. Öztürk, B.E., Johnson, M.E., Kleyman, M., Turunç, S., He, J., Jabalameli, S., Xi, Z., Visel, M., Dufour, V.L., Iwabe, S., et al. (2021). scAAVengr, a transcriptome-based pipeline for quantitative ranking of engineered AAVs with single-cell resolution. eLife *10*, e64175. https://doi.org/10.7554/elife.64175.

32. Jung, N., and Kim, T.-K. (2023). Spatial transcriptomics in neuroscience. Exp. Mol. Med. *55*, 2105–2115. https://doi.org/10.1038/s12276-023-01093-y.

33. Tian, L., Chen, F., and Macosko, E.Z. (2023). The expanding vistas of spatial transcriptomics. Nat. Biotechnol. *41*, 773–782. https://doi.org/10.1038/s41587-022-01448-2.

34. Park, H.E., Jo, S.H., Lee, R.H., Macks, C.P., Ku, T., Park, J., Lee, C.W., Hur, J.K., and Sohn, C.H. (2023). Spatial Transcriptomics: Technical Aspects of Recent

Developments and Their Applications in Neuroscience and Cancer Research. Adv. Sci. *10*, 2206939. https://doi.org/10.1002/advs.202206939.

35. Coughlin, G.M., Borsos, M., Barcelona, B.H., Appling, N., Mayfield, A.M.H., Mackey, E.D., Eser, R.A., Jackson, C.R., Chen, X., Kumar, S.R., et al. (2026). Spatial genomics of AAV vectors reveals mechanism of transcriptional crosstalk that enables targeted delivery of large genetic cargo. Nat. Biotechnol. *44*, 133–145. https://doi.org/10.1038/s41587-025-02565-4.

36. Jang, M.J., Coughlin, G.M., Jackson, C.R., Chen, X., Chuapoco, M.R., Vendemiatti, J.L., Wang, A.Z., and Gradinaru, V. (2023). Spatial transcriptomics for profiling the tropism of viral vectors in tissues. Nat. Biotechnol. *41*, 1272–1286. https://doi.org/10.1038/s41587-022-01648-w.

37. Bell, C.L., Gurda, B.L., Van Vliet, K., Agbandje-McKenna, M., and Wilson, J.M. (2012). Identification of the Galactose Binding Domain of the Adeno-Associated Virus Serotype 9 Capsid. J. Virol. *86*, 7326–7333. https://doi.org/10.1128/jvi.00448-12.

38. Huang, Q., Chan, K.Y., Tobey, I.G., Chan, Y.A., Poterba, T., Boutros, C.L., Balazs, A.B., Daneman, R., Bloom, J.M., Seed, C., et al. (2019). Delivering genes across the blood-brain barrier: LY6A, a novel cellular receptor for AAV-PHP.B capsids. PLoS One *14*, e0225206. https://doi.org/10.1371/journal.pone.0225206.

39. Hordeaux, J., Yuan, Y., Clark, P.M., Wang, Q., Martino, R.A., Sims, J.J., Bell, P., Raymond, A., Stanford, W.L., and Wilson, J.M. (2019). The GPI-Linked Protein LY6A Drives AAV-PHP.B Transport across the Blood-Brain Barrier. Mol. Ther. *27*, 912–921. https://doi.org/10.1016/j.ymthe.2019.02.013.

40. Fang, K., Yang, X., Liu, Y., Xia, J., Wu, R., Yang, F., Feng, C., Liu, X., Shi, L., Geng, G., et al. (2025). A comprehensive study of AAV tropism across C57BL/6 mice, BALB/c mice, and crab-eating macaques. Mol. Ther. Methods Clin. Dev. *33*, 101434. https://doi.org/10.1016/j.omtm.2025.101434.

41. Yao, Z., van Velthoven, C.T.J., Nguyen, T.N., Goldy, J., Sedeno-Cortes, A.E., Baftizadeh, F., Bertagnolli, D., Casper, T., Chiang, M., Crichton, K., et al. (2021). A taxonomy of transcriptomic cell types across the isocortex and hippocampal formation. Cell *184*, 3222–3241.e26. https://doi.org/10.1016/j.cell.2021.04.021.

42. Yao, Z., van Velthoven, C.T.J., Kunst, M., Zhang, M., McMillen, D., Lee, C., Jung, W., Goldy, J., Abdelhak, A., Aitken, M., et al. (2023). A high-resolution transcriptomic and spatial atlas of cell types in the whole mouse brain. Nature *624*, 317–332. https://doi.org/10.1038/s41586-023-06812-z.

43. Harris, J.A., Mihalas, S., Hirokawa, K.E., Whitesell, J.D., Choi, H., Bernard, A., Bohn, P., Caldejon, S., Casal, L., Cho, A., et al. (2019). Hierarchical organization of cortical and thalamic connectivity. Nature *575*, 195–202. https://doi.org/10.1038/s41586-019-1716-z.

44. Cembrowski, M.S., and Spruston, N. (2019). Heterogeneity within classical cell types is the rule: lessons from hippocampal pyramidal neurons. Nat. Rev. Neurosci. *20*, 193–204. https://doi.org/10.1038/s41583-019-0125-5.

45. Okamoto, K., Kamikubo, Y., Yamauchi, K., Okamoto, S., Takahashi, M., Ishida, Y., Koike, M., Ikegaya, Y., Sakurai, T., and Hioki, H. (2023). Specific AAV2/PHP.eB-mediated gene transduction of CA2 pyramidal cells via injection into the lateral ventricle. Sci. Rep. *13*, 323. https://doi.org/10.1038/s41598-022-27372-8.

46. Bunuales, M., Garduno, A., Chillon, M., Bosch, A., Gonzalez-Aparicio, M., Espelosin, M., Garcia-Gomara, M., Rico, A.J., Garcia-Osta, A., Cuadrado-Tejedor, M., et al. (2024). Characterization of brain transduction capability of a BBB-penetrant AAV vector in mice, rats and macaques reveals differences in expression profiles. Gene Ther. *31*, 455–466. https://doi.org/10.1038/s41434-024-00466-w.

47. Yao, Y., Wang, J., Liu, Y., Qu, Y., Wang, K., Zhang, Y., Chang, Y., Yang, Z., Wan, J., Liu, J., et al. (2022). Variants of the adeno-associated virus serotype 9 with enhanced penetration of the blood–brain barrier in rodents and primates. Nat. Biomed. Eng. *6*, 1257–1271. https://doi.org/10.1038/s41551-022-00938-7.

48. Chatterjee, D., Marmion, D.J., McBride, J.L., Manfredsson, F.P., Butler, D., Messer, A., and Kordower, J.H. (2022). Enhanced CNS transduction from AAV.PHP.eB infusion into the cisterna magna of older adult rats compared to AAV9. Gene Ther. *29*, 390–397. https://doi.org/10.1038/s41434-021-00244-y.

49. Mathiesen, S.N., Lock, J.L., Schoderboeck, L., Abraham, W.C., and Hughes, S.M. (2020). CNS Transduction Benefits of AAV-PHP.eB over AAV9 Are Dependent on Administration Route and Mouse Strain. Mol. Ther. Methods Clin. Dev. *19*, 447–458. https://doi.org/10.1016/j.omtm.2020.10.011.

50. Nieuwenhuis, B., Haenzi, B., Hilton, S., Carnicer-Lombarte, A., Hobo, B., Verhaagen, J., and Fawcett, J.W. (2021). Optimization of adeno-associated viral vector-mediated transduction of the corticospinal tract: comparison of four promoters. Gene Ther. *28*, 56–74. https://doi.org/10.1038/s41434-020-0169-1.

51. Dogbevia, G.K., Töllner, K., Körbelin, J., Bröer, S., Ridder, D.A., Grasshoff, H., Brandt, C., Wenzel, J., Straub, B.K., Trepel, M., et al. (2017). Gene therapy decreases seizures in a model of Incontinentia pigmenti. Ann. Neurol. *82*, 93–104. https://doi.org/10.1002/ana.24981.

52. Kawabata, H., Konno, A., Matsuzaki, Y., and Hirai, H. (2023). A blood-brain barrier-penetrating AAV2 mutant created by a brain microvasculature endothelial cell-targeted AAV2 variant. Mol. Ther. Methods Clin. Dev. *29*, 81–92. https://doi.org/10.1016/j.omtm.2023.02.016.

53. Grimm, D., and Nonnenmacher, M. (2023). Every little bit helps: A single-residue switch in a vascular AAV enables blood-brain barrier penetration. Mol. Ther. Methods Clin. Dev. *29*, 364–365. https://doi.org/10.1016/j.omtm.2023.04.007.

54. Nucera, M., Charitakis, N., Leung, R., Leichter, A., Tuano, N., Walkiewicz, M., Sawant, V., Rowley, L., Scurr, M., Er, P., et al. (2025). Application of spatial transcriptomics across organoids: a high-resolution spatial whole-transcriptome benchmarking dataset. Preprint at bioRxiv. https://doi.org/10.1101/2025.05.04.651803.

55. Depla, J.A., Sogorb-Gonzalez, M., Mulder, L.A., Heine, V.M., Konstantinova, P., van Deventer, S.J., Wolthers, K.C., Pajkrt, D., Sridhar, A., and Evers, M.M. (2020). Cerebral Organoids: A Human Model for AAV Capsid Selection and Therapeutic Transgene Efficacy in the Brain. Mol. Ther. Methods Clin. Dev. *18*, 167–175. https://doi.org/10.1016/j.omtm.2020.05.028.

56. Strobel, B., Zuckschwerdt, K., Zimmermann, G., Mayer, C., Eytner, R., Rechtsteiner, P., Kreuz, S., and Lamla, T. (2019). Standardized, Scalable, and Timely Flexible Adeno-Associated Virus Vector Production Using Frozen High-Density HEK-293 Cell Stocks and CELLdiscs. Hum. Gene Ther. Methods *30*, 23–33. https://doi.org/10.1089/hgtb.2018.228.

57. Hao, Y., Stuart, T., Kowalski, M.H., Choudhary, S., Hoffman, P., Hartman, A., Srivastava, A., Molla, G., Madad, S., Fernandez-Granda, C., et al. (2024). Dictionary learning for integrative, multimodal and scalable single-cell analysis. Nat. Biotechnol. *42*, 293–304. https://doi.org/10.1038/s41587-023-01767-y.